MDPI

Microstructure and Properties of Wire Arc Additive Manufacturing of Inconel 625

Odd M. Akselsen [1], Ruben Bjørge [1] , Håkon Wiik Ånes [2] , Xiaobo Ren [1],* and Bård Nyhus [1]

[1] Department of Materials and Nanotechnology, SINTEF Industry, 7465 Trondheim, Norway
[2] Department of Materials Science and Engineering, Norwegian University of Science and Technology, 7491 Trondheim, Norway
* Correspondence: xiaobo.ren@sintef.no

Abstract: In the present investigation, wire arc additive manufacturing of Inconel 625 was carried out with the cold metal transfer variant of the metal inert gas process. The heat input varied between 0.46 and 0.63 kJ/mm, which is a rather low heat input with low deposition rate. The built walls were subjected to Charpy V and crack tip opening displacement (CTOD) fracture toughness testing, in addition to microstructure examination with light microscope and scanning and transmission electron microscope. The results obtained show that hardness increases from the base metal level of 210, via the heat-affected zone (in the building plate) with HV of 220, to the weld metal, with a hardness of around 240–250. All individual Charpy V values fall within the range from 160 to 200 J, while the CTOD fracture toughness is within the range from 0.49 to 1.05 mm. The microstructure examination revealed the microsegregation of certain elements to the interdendritic regions, causing three different particle types to form. Particles with a spherical morphology were identified as spinel ($MgAl_2O_4$). Some of the spinel particles were surrounded by disc-shaped precipitates, which were identified as (NbTi)(CN), having the same orientation as the spinel.

Keywords: wire arc additive manufacturing; nickel superalloy; mechanical properties; microstructures; microsegregation

1. Introduction

Additive manufacturing (AM), or 3D printing, represents a relatively new method for the production of components and parts. Compared with powder-based AM techniques, which usually employ laser beams and electron beams as heat sources, Martina et al. [1], Szoost et al. [2], and Williams et al. [3] all found that wire arc additive manufacturing (WAAM) [4] shows advantages for the manufacture of large-scale components due to its high deposition rate, high material use rate, low production and equipment cost, and high equipment flexibility and scalability. This is in contrast to conventional subtractive production involving casting and/or forming with final cutting and machining with the removal of excess material from the final product.

WAAM can be applied for most metals and alloys that are weldable with fusion welding techniques. However, the product design may influence the deposition parameters to be used, restricting the operation window. Another challenge is anisotropy in mechanical properties. Several processes can be used in WAAM. Fang et al. [5,6] employed the cold metal transfer (CMT) process using different arc modes in the deposition of AA2219 and AA5183 alloys. The authors reported that pulse advanced CMT (CMT-PADV) and advanced CMT (CMT-ADV), respectively, appeared to give the highest strength for the two alloys. Similar studies were carried out by Cong et al. [7,8], with the lowest porosity being obtained when using advanced CMT (CMT+ADV). Horgar et al. [9] reported mechanical test data from WAAM of AA5183 using conventional gas metal arc welding (GMAW), demonstrating that quite good mechanical properties can be achieved despite the fact that porosity and

some hot cracking may arise. A major and still not solved problem for aluminium alloys is the limited commercial availability of wires, which may limit the use of WAAM of Al alloys.

By contrast, WAAM of titanium alloys has been demonstrated using a rapid plasma deposition (RPD) process (Norsk Titanium). Martina et al. [1] demonstrated that a plasma wire deposition process was able to produce straight walls of Ti–6Al–4V alloy with widths of up to 17.4 mm, giving a maximum effective wall width after machining of 15.9 mm. In addition, they reported a micro-hardness value of 387 HV, which was 12% higher than that of the substrate. Wu et al. [10] investigated the influence of heat accumulation on bead formation, arc stability, and metal transfer behaviour during the manufacture of Ti6Al4V with the gas tungsten wire arc additive manufacturing (GT-WAAM) using localized gas shielding. Owing to the influences of heat accumulation, the interlayer surface oxidation and bead geometries varied along the building direction, especially for the first few layers of the deposited wall, leading to variation in arc shape and metal transfer behaviour. Martina et al. [11] examined the effect of high-pressure interpass rolling after six passes of deposition using GT-WAAM. The microstructure changed from large columnar prior β grains traversing the component to equiaxed grains. In metals with an absence of solid-state phase transformation, epitaxial solidification provides grains growing throughout the individual layers.

In addition to light metals like aluminium and titanium alloys, both nickel superalloys and austenitic stainless steels have been subjected to WAAM. For the latter material, type 304 austenitic stainless steel was studied by Haden et al. [12]. They found that the wear rate declined in the direction of weld deposition, indicating that material wear resistance and strength were graded along the deposition path. Anisotropy in strength was also found by Ji et al. [13], which was explained by different grain boundary strengthening effects between the transverse direction and the longitudinal direction. Rodriguez et al. [14] manufactured 316L grade austenitic stainless steel using the CMT and TopTIG (tungsten inert gas) processes. After process optimization, the authors reported material deposition rates of up to 3.7 kg/h and above 2 kg/h for CMT and TopTIG, respectively. They found some anisotropy in mechanical properties in the as-built state, with lower strength values in the vertical (Z) orientation. WAAM of 17–4 PH martensitic stainless steel was reported by Martina et al. [15], where solution heat treatment after completion of deposition was found to increase the strength to the base plate level. Caballero et al. [16] showed that direct aging solution treatment resulted in a reduction in ductility by nearly 50%, possibly due to the formation of intermetallic phases.

Duplex stainless steel is a popular material for oil and gas applications, but there are very limited results available from additive manufacturing. Eriksson et al. [17] concluded that additive manufacturing of superduplex stainless steels by the wire and arc process is feasible. Their microstructure observations consisted of low ferrite volume fraction, precipitation of Cr nitrides in the heat-affected zone (HAZ) towards the support plate and formation of secondary austenite in reheated areas. Recent results by Akselsen et al. [18], using elevated temperature between the deposition of each layer to increase productivity clearly demonstrated the harmful effects of sigma phase formation on the toughness of WAAM samples.

Ni-based superalloys are widely applied in the aeronautical, aerospace, chemical, petrochemical and marine industries. They are also popular in the oil and gas industry due to their good resistance to high-temperature corrosion on prolonged exposure to aggressive environments, as noticed by Shankar et al. [19,20] and Xu et al. [21]. One example is the 718 study by Asala et al. [22], which demonstrated extensive formation of eutectic solidification microconstituents including Laves and MC-type carbide phases due to the microsegregation of Nb. The γ' (Ni_3Al) is the primary precipitation strengthening phase in this alloy. Although the Ni-based alloys were developed for high-temperature applications, they have excellent corrosion properties, which made them popular in the oil and gas industry. This is a precipitation hardening alloy, where the strength is derived from the precipitation of fine γ', Nb_3Al, and γ'', Nb_3Nb. Such precipitates have been identified by

Cozar and Pineau [23], Xie et al. [24] and Asala et al. [22]. One perhaps more frequently used alloy is Inconel 625, which, in contrast to alloy 718, receives its strength from solid solution strengthening. Due to the high costs of these alloys and the minimum lead time for replacing damaged parts, the development of additive manufacturing processes may contribute to shortening the time required for replacement. Moreover, preventative maintenance and design changes/upgrades, or even online repair and refurbishment of eroded/corroded or cracked components may be feasible, and may be much more cost effective than full replacement. Due to the complex shape of such components, direct metal deposition (DMD) techniques for Inconel 625 components have attracted increasing attention, as discussed by Thivillon et al. [25].

WAAM represents a clear alternative to powder bed fusion (PBF) and DMD, using various alternative process options that may also provide high productivity beyond that of laser-assisted powder melting methods, but which may not produce details that are as complex, and which needs machining post layer deposition. In the present study, WAAM of Inconel 625, using the cold metal transfer (CMT) variant of gas metal arc welding (GMAW), is performed with the objective of assessing microstructure and toughness properties after wall deposition. Today, such data are very scarce; in particular, impact and fracture toughness data are lacking. An attempt is also made to compare current results with the hardness and toughness achieved using other AM processes.

2. Materials and Methods

2.1. Materials

The nickel-based superalloy Inconel 625 was selected for the present study. This is a Ni-Cr-Mo-Nb alloy supplied in the form of wire with a diameter of 1.2 mm. The support plate was also Inconel 625. The alloy contains minimum 58% Ni with 20–23% Cr and 8–10% Mo (see Table 1). Some microalloying elements may also be found in some alloys, like Ti and Al. Its melting temperature is in the range of 2350–2460 °C, depending on the chemical composition. Both yield and tensile strength of the material vary within a wide range, depending on the production route and heat treatment practice.

Table 1. Nominal chemical composition of Inconel 625 wire.

Ni	Cr	Mo	Fe	Nb	C	Mn	Si	P	S
>58.0	20.0–23.0	8.0–10.0	< 5.0	3.15–4.15	<0.10	<0.50	<0.50	<0.015	<0.015

2.2. Deposition of Walls

The deposition of walls was carried out with a CMT power source (Fronius Norge AS, Hokksund, Norway), which is a special type of gas metal arc welding (GMAW) providing lower heat input. The parameters used are outlined in Table 2. The heat input was varied from 0.36 to 0.76 kJ/mm and was adjusted by increasing/decreasing current. Thus, the heat input was very low for all deposited layers. In addition, the interpass temperature varied; the higher the heat input, the higher the interpass temperature. The deposition results are seen in Table 3, indicating that all walls had 16 layers with average layer heights varying from 2.5 to 2.8 mm. As expected, the layer height (and width) increased with increasing heat input.

Table 2. Layer deposition parameters.

Parameter	Wall No.		
	W1	W2	W3 and W4
Current (A)	231	201	139
Voltage (V)	21	20	17
Travel speed (mm/s)	7.0	7.0	7.0
Wire speed (mm/s)	12.7	10.3	6.7
Heat input (kJ/mm)	0.76	0.62	0.36
Average interpass temperature (°C)	152	140	85
Polarity	DC+	DC+	DC+

Table 3. Deposition results.

Wall Production Data	Wall No.		
	W1	W2	W3 and W4
Number of layers	16	16	16
Average layer height (mm)	2.8	2.7	2.5
Wall width (mm)	11.8	10.2	7
Wall length (mm)	230	230	230

2.3. Testing and Characterization

The walls were cut perpendicular to the deposition direction to prepare cross-section macrographs for visual inspection, hardness measurements (Zwick Roell ZHV30 A, Zwick Roell GmbH, Ulm, Germany) and microstructure characterization. Three subsized Charpy V samples with a cross-section of 5 mm × 10 mm and a length of 55 mm were cut from the walls, with their length axes parallel to the deposition direction. Three CTOD (Crack Tip Opening Displacement) specimens were also cut from the walls, with the same cross-sections as the Charpy V samples. Both Charpy and CTOD specimens were tested at a temperature of −46 °C.

Microstructure characterization was carried out with light microscopy, scanning electron microscopy (SEM) and transmission electron microscopy (TEM). SEM imaging and chemical analysis using energy-dispersive X-ray spectroscopy (EDX) was performed using an FEI Apreo (Thermo Fisher Scientific, Waltham, MA, USA). Electron backscattered diffraction was performed in a Hitachi SU-6600 SEM (Hitachi High-Tech Corporation, Tokyo, Japan). Scanning TEM (STEM) EDX point analysis and selected-area electron diffraction (SAED) was performed in a JEOL JEM-2100F TEM (JEOL Ltd., Tokyo, Japan), while simultaneous EDX and electron energy-loss spectroscopy (EELS) mapping was performed in an aberration-corrected JEOL ARM 200F (JEOL Ltd., Tokyo, Japan), all at 200 kV. SEM and TEM specimens were prepared in the final step by electropolishing, except for before the EBSD analysis, in which case polishing with a colloidal silica suspension was done in the final step to obtain a flat surface.

Hough indexing of EBSD patterns was performed with the EDAX TSL OIM DC software (v7.3, EDAX, Mahwah, NJ, USA). Dictionary indexing (DI) of EBSD patterns [26] was performed with the open-source kikuchipy Python library [27], using dynamically simulated master patterns and orientation sampling obtained with EMsoft v5.0 [28,29]. Dictionaries of simulated patterns were populated by orientations sampled with an average angular step size of 1.4°. Patterns were projected from master patterns in the square Lambert projection onto the detector using bi-quadratic interpolation with a fixed projection centre. Static and dynamic background corrections were performed on experimental patterns prior to indexing. Experimental and dictionary patterns were compared using the normalized cross-correlation (NCC) coefficient, *r*. Final orientation refinement of the best match in the dictionary to each experimental pattern was done through optimization of the NCC score using the Nelder–Mead algorithm, implemented in SciPy [30].

## 3. Results and Discussion

3.1. Macroscopic Examination

The macrographs of wall cross-sections are shown in Figure 1. The walls were free from weld defects, but had some distortion.
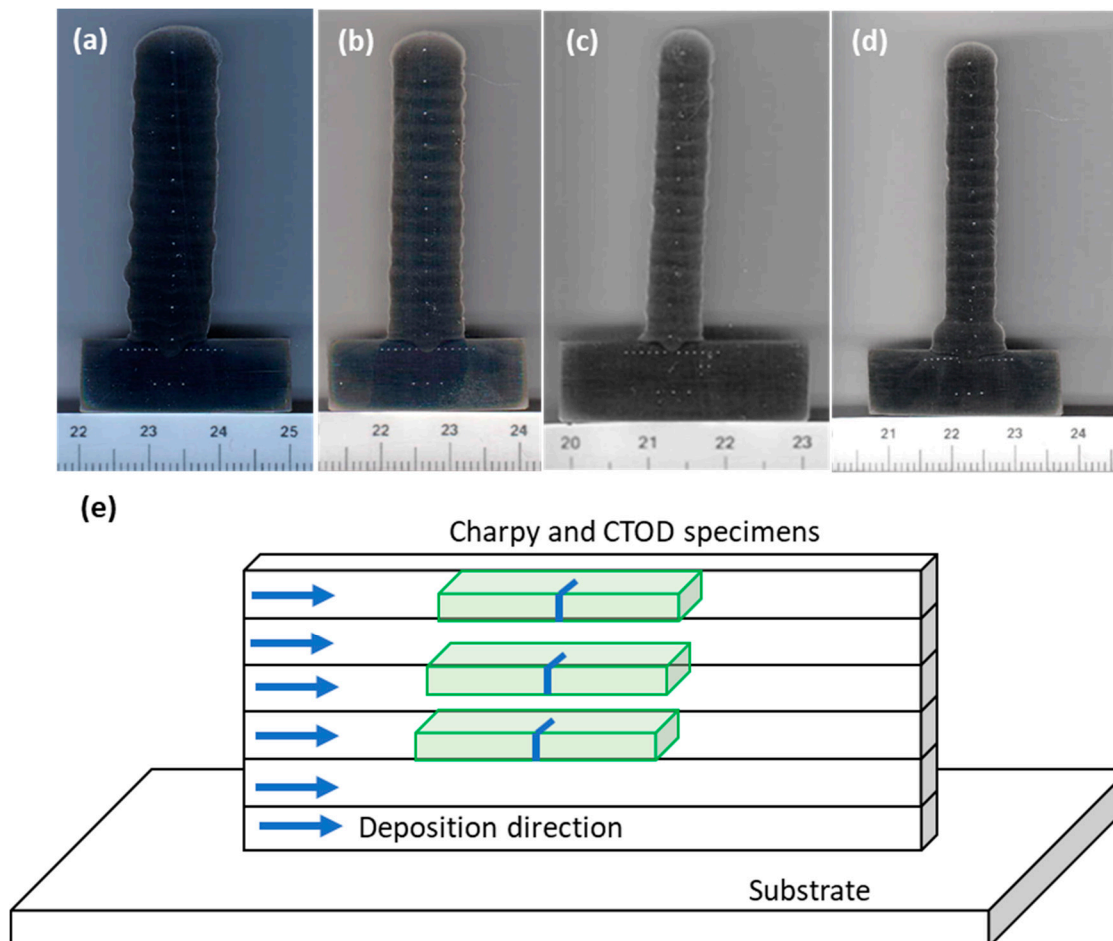
Figure 1. Macrographs of walls (cross-sections, ruler scale in centimeters). (**a**) W1—0.76 kJ/mm; (**b**) W2—0.62 kJ/mm; (**c,d**) W3 and W4—0.3–0.4 kJ/mm. (**e**) Schematic illustration of the walls with the Charpy and crack tip opening displacement (CTOD) specimens indicated.

3.2. Hardness

The hardness was measured along the vertical line along the centreline of the wall (the hardness indentations are shown as white spots in the macrographs in Figure 1). It can be seen from the data presented in Figure 2 that the employed heat input range does not alter the hardness level much, either in the HAZ or the deposited layers. The hardness increases from the base metal level of 210, via the HAZ with HV of 220 to the fused metal with a hardness of around 240–250. The base metal hardness is the lowest of all regions; probably due to the fact that plates of Inconel 625 are normally heat treated (to reduced hardness level) to achieve more homogeneous properties throughout the material. The hardness of the support plate increases in the HAZ due to the rapid heating and cooling cycle. This seems to be sufficient for dissolution and reprecipitation of the strength-enhancing NbC.
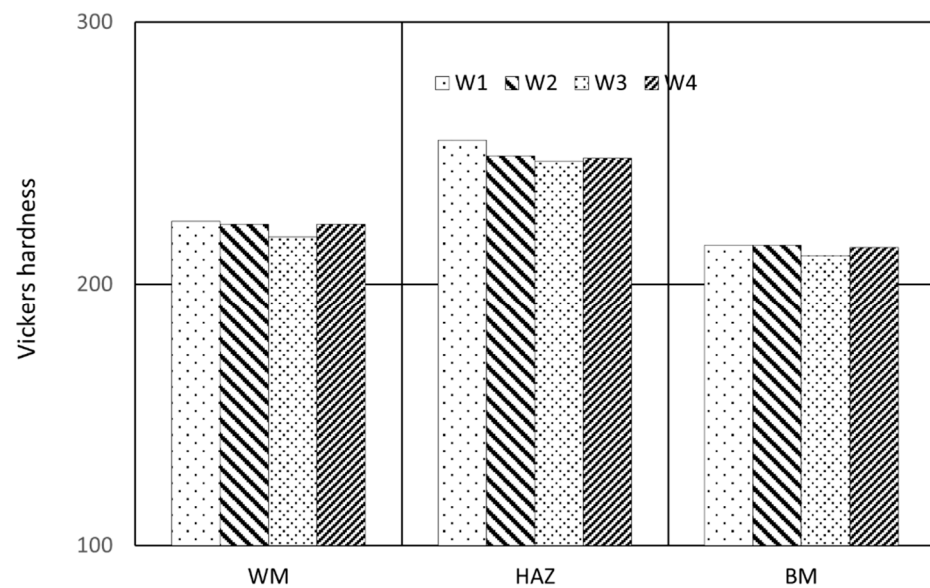
Figure 2. Maximum hardness distribution. WM: weld metal, HAZ: heat-affected zone, BM: base metal.

The hardness of the deposited layers falls in the same range as the results published by Dinda et al. based on deposition with a 6 kW CO2 laser using a laser power of 600–900 W [31]. Similar levels were reported in CMT-WAAM experiments by Wang et al. [32]. The measured HV corresponds to single-pass pulsed current gas tungsten arc welding (PCGTAW), as recently found by Korropati et al. [33].

The hardness level seems to be lower than that reported by Xu et al. using pulsed plasma arc deposition AM, where a hardness of 294 was reported [34]. The authors increased the hardness to 342 following stepwise heat treatment with solution treatment at 980 °C for 1 h. In another study by these authors, a hardness in the range 260–280 was reported [35]. According to Wang et al., based upon gas tungsten arc AM, the microhardness tends to vary somewhat within different regions, ranging from 240 to 270 HV [36].
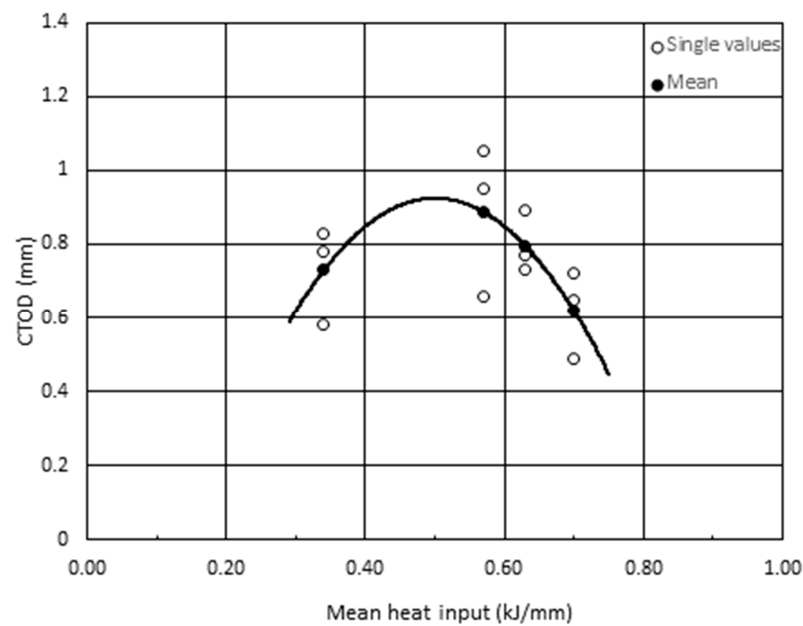
3.3. Toughness

The Charpy V toughness at −46 °C is plotted versus heat input in Figure 3. All individual values fall within the range from 160 to 200 J, which is excellent. It is difficult to find published literature on the WAAM of Inconel 625 that also addresses impact toughness properties. However, Paul et al. published room temperature Charpy V values from powder baser laser manufacturing [37]. Their results were all between 100 and 110 J. Even lower values were achieved by Puppala et al. in laser manufacturing, reporting values of 48–50 J in the as-deposited state, and 50–54 J after stress relieving heat treatment (at 950 °C for one hour followed by oil quenching) [38]. The authors did not report the test temperature, so it is reasonable to assume that this was performed at room temperature. The comparison clearly demonstrates the potential of the employed WAAM process and parameters in making components in this alloy. The toughness is difficult to relate directly to the microstructure, since the test samples comprise both nonreheated and reheated areas. One may expect that the samples with the most reheated areas would offer better toughness due to the more homogeneous material. In practice, this point is difficult to verify experimentally.
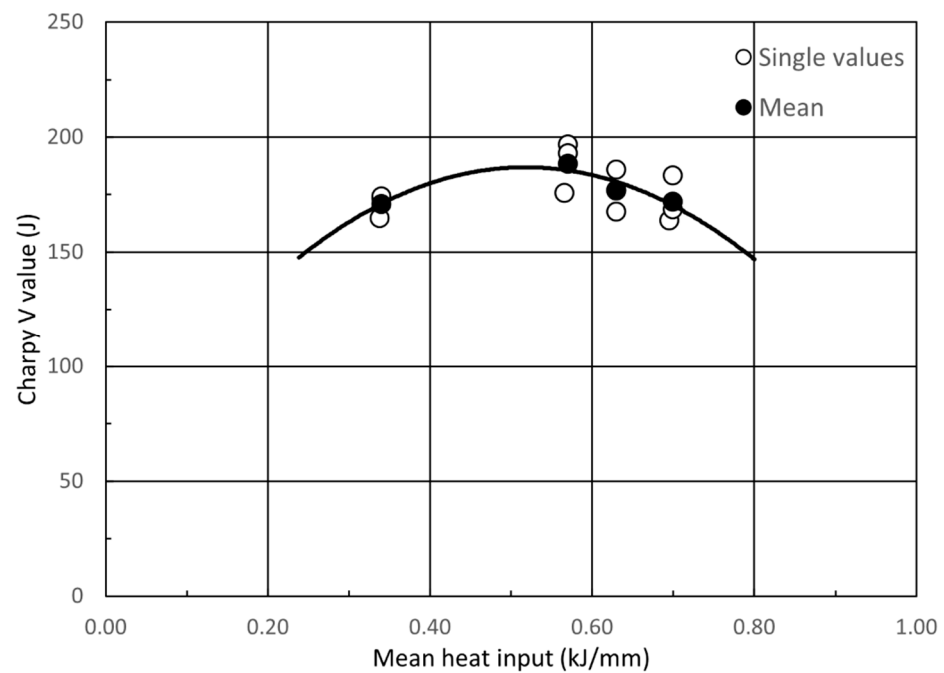
Figure 3. Charpy V toughness at −45 °C.

The results for the CTOD fracture mechanics specimens are outlined in Figure 4. It was found that the CTOD values obtained at −46 °C fall within the range from 0.49 to 1.05 mm. The average value seems to deteriorate with increasing heat input. Fortunately, CTOD test results have been published previously for WAAM of Inconel 625. Puppala et al. [38] reported a similar test set-up using laser-based (2.8–3.0 kW laser power) additive manufacturing with powder, with CTOD values in the as-deposited state in the range of 0.28–0.4 mm, which is somewhat lower than those in the present investigation. Even after post-deposition heating, the values were in the range of 0.34–0.54 mm, which is still below the data set presented in Figure 4. Cam et al. reported weld metal fracture toughness of laser-welded Inconel 625 sheets in the range of 0.48–0.54 mm [39], whereas Yeni and Kocak reported somewhat higher values of 0.53–0.88 mm [40]. Cam et al. reported that the values for their 625 alloy in the wrought form were about 1.03–1.16 mm [39]. Considering that all these values were obtained at room temperature, the developed layer deposition process appeared to offer excellent toughness. It is to be noted that specimen thickness strongly influences fracture toughness, as mode of fracture undergoes a transition from plane stress to plane strain conditions (with an associated increase in the constraint at the crack tip) with increasing thickness. In the present work, samples of 5 mm were used, which is smaller than in the work by Cam et al. [39].

Figure 4. CTOD fracture toughness at −45 °C.

3.4. Optical Microscopy

The microstructures of the different walls were examined using a light microscope. Starting with the building plate, the microstructure is shown in Figure 5. It can be seen that the grain size is large, with some grains even approaching 100 μm. They are polygonal in shape. Another feature is that the solidification microstructure is revealed with interdendritic segregation, including particle alignment. The width of these regions seems to vary between ~12 and 30 μm, and they are separated by an average centre-to-centre distance of 62 μm (primary dendrite spacing). The polygonal grains are formed in the Liq → γ reaction, while microsegregation takes place for the elements Cr, Mo, Nb to the interdendritic regions, which will be the last to solidify through the reaction Liq → γ + Laves. Banded microstructures of this type may display very poor ductility when strained perpendicular to the bands [41]. However, no Laves phase was found in the present investigation, which may be connected to the low heat input employed in wall deposition.
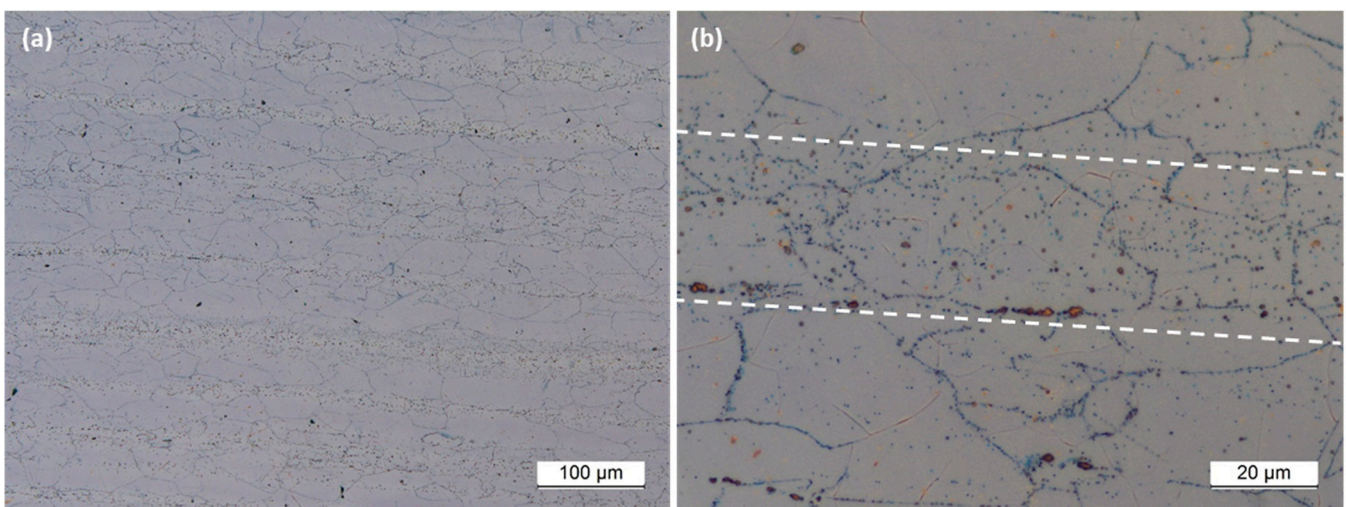
Figure 5. Building plate microstructure. (**a**) overview, (**b**) close-up showing numerous particles in a former interdendritic region (between the white lines).

After deposition of the first layer, the heat-affected zone (HAZ) is formed in the building plate similar to a HAZ in welding. The microstructure is shown in Figure 6, and indicates clear changes upon reheating when compared with the base plate. Brownish/yellowish regions form that contain intermetallic compounds (discussed below). The higher the peak temperature in reheating, the denser these regions will be. These are formed in a matrix of γ grains of polygonal shape. Apparently, these colonies are not aligned although they seem to follow the initial segregation pattern, and form arbitrarily at grain boundaries or the grain interior. No grain coarsening takes place in the HAZ due to the large initial size, offering low driving force for grain growth. Another important observation is that the HAZ has a maximum width of 200 μm, due to the low heat input employed and the low thermal conductivity in the alloy. W1 and W2 have even smaller widths, approaching 100 μm in the case of the latter.
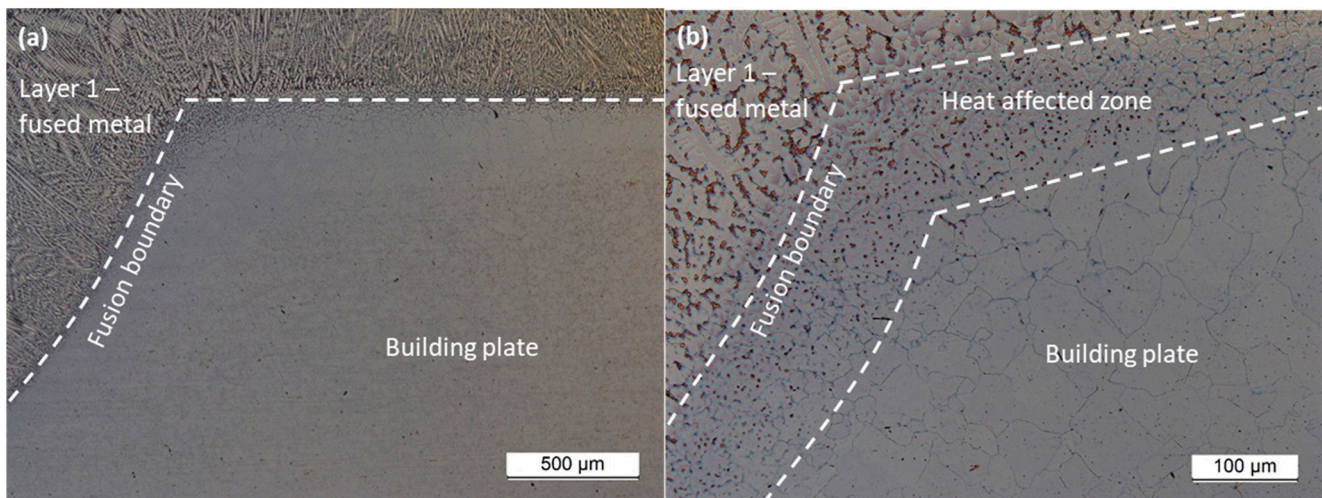

Figure 6. HAZ region towards the building plate. (**a**) overview and (**b**) close-up of W1.

The microstructure of the fused zone is shown in Figure 7 for W1 as an example. It is evident that columnar dendritic solidification takes place. This means that primary dendrites of the γ phase nucleate and grow, with heavy microsegregation of elements like Mo and Nb to liquid interdendritic regions. As expected, the primary dendrite spacing is substantially refined compared with the building plate. This is linked to much faster cooling rates involved in layer deposition than in the production of the building plate.
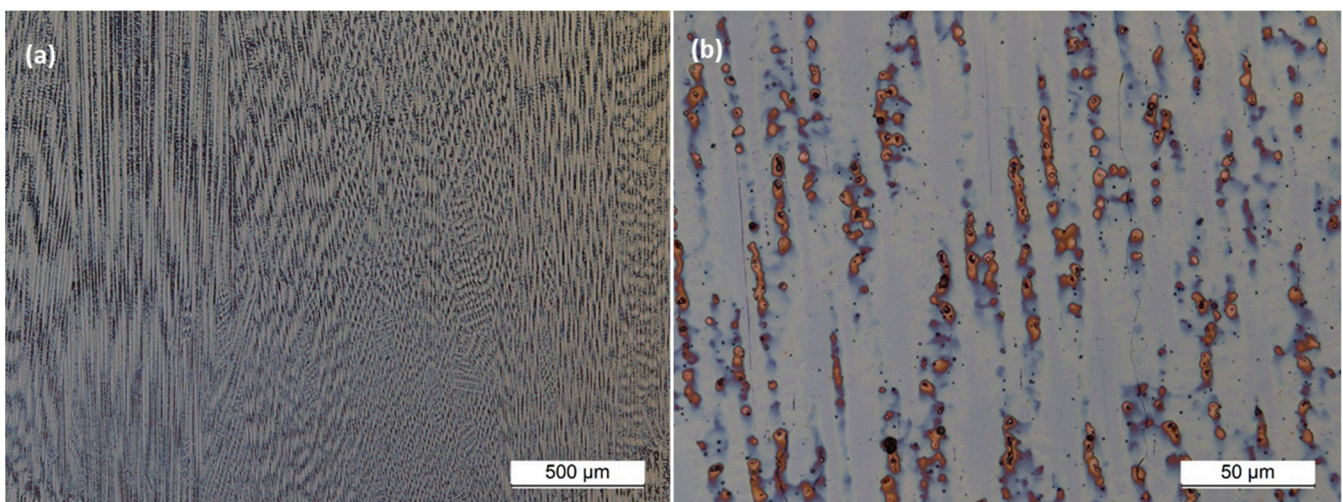

Figure 7. Primary (not reheated) fused metal of W1. (**a**) overview, (**b**) close-up.

The primary dendrite spacing was also measured after layer deposition. These measurements were not straightforward, due to the columnar form of dendrites. It was decided to carry out the measurements using micrographs taken at an intermediate magnification (200X) in order to see clear details while still having an overview of the solidification structure. The results are plotted in Figure 8. After layer deposition, the as-fused metal has a primary dendrite arm spacing within the range of 9 to 18 μm with a standard deviation of 2.1–3.1 μm. For the reheated part of the layer, the spacing varied between 8 and 23 μm, with an associated standard deviation of 2.9–4.2 μm. As is evident from Figure 8, there is no unambiguous trend in the effects of heat input on dendrite arm spacing. However, there is a clear indication that the dendrite arm spacing increases after reheating. This observation is substantiated by the micrograph contained in Figure 9. The top of the micrograph shows a new layer consisting of a primary part and a part reheated at high temperature, while the bottom area is unaffected layer due to lower temperature. The alloy melts at about 1350 °C and starts to solidify at ~1290 °C [42].
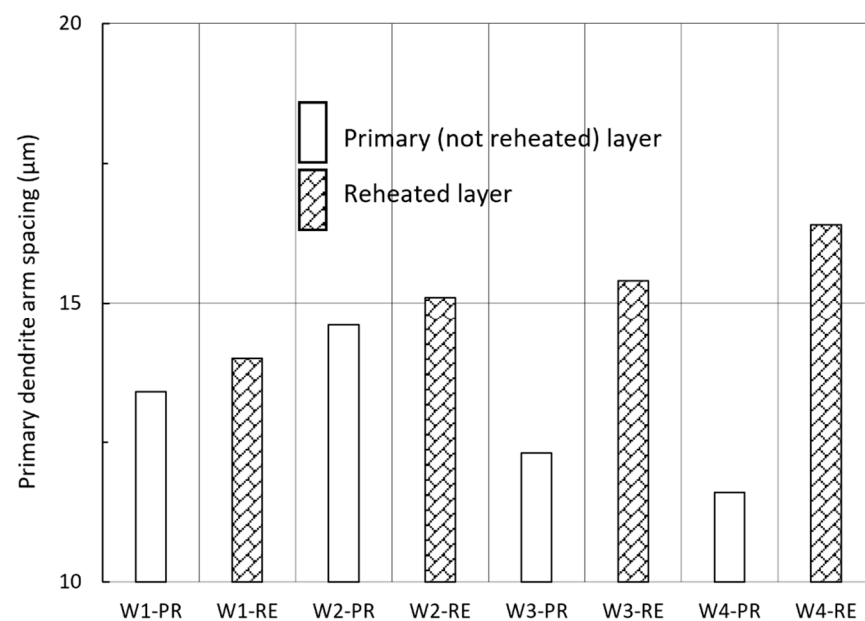

Figure 8. Primary dendrite arm spacing. PR is the primary deposited layer, while RE denotes the reheated part of layer.
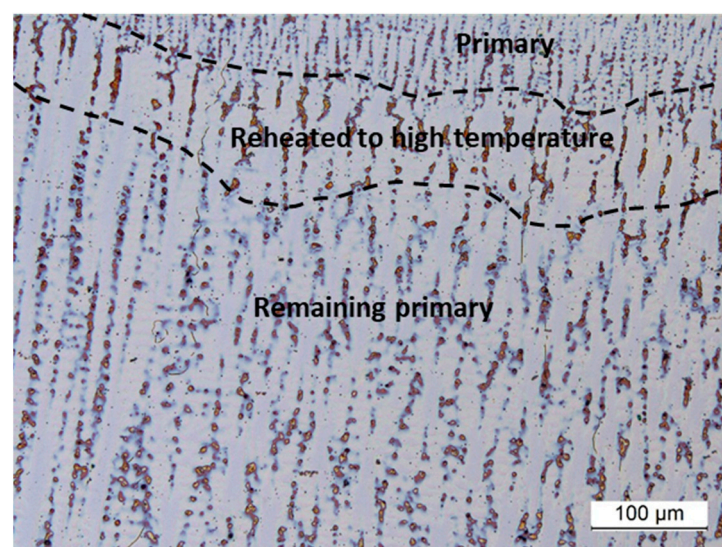
Figure 9. Dendrites in primary and reheated layers, W3.

3.5. SEM and TEM Observations

SEM and TEM samples were prepared from the middle of the wall cross-sections. Figure 10 shows a backscattered electron (BSE) image and corresponding EDX elemental maps from a typical region in the middle of W1. The microstructure is quite similar to the optical microscopy image shown in Figure 7b. The interdendritic regions are brighter in the BSE image since they are enriched with Nb and Mo. The values of the partition coefficient k for Mo and Nb are lower than 1. Thus, these elements segregate during solidification into the liquid and hence, when solidification is completed, the inter-dendritic regions are considerably enriched with Nb and Mo. By contrast, Ni, Cr and possibly Fe have partition coefficients above 1, and are therefore enriched in the primary dendrite arms. The elemental maps show that there are also some particles rich in Nb and some rich in Al, mainly in interdendritic regions. The "flower-like" features in the BSE image had a composition identical to that of the surrounding matrix. It was therefore concluded that these features are artefacts of the electropolishing.
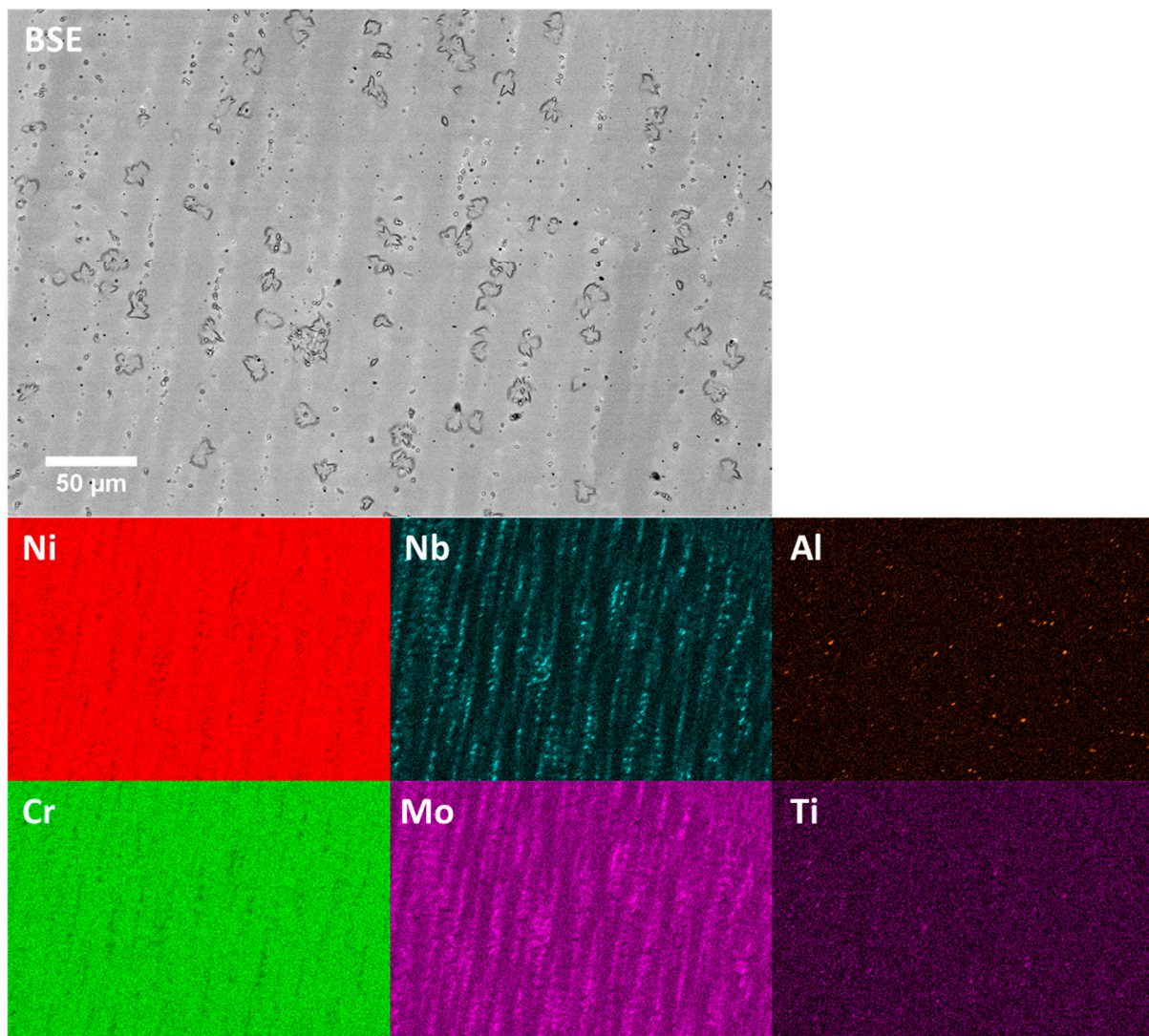

Figure 10. SEM EDX map of a region near the middle of W1. The interdendritic regions are rich in Nb and Mo. Particles rich in Nb and some rich in Al can also be seen.

Figure 11 gives a more detailed view of an SEM sample taken from the middle of W3. The EDX analysis confirms that the interdendritic regions are enriched with Nb and Mo.

The SEM-EDX spectra from the particles indicate that some particles are rich in Al, and dark in the BSE image, while brighter particles are rich in Nb.

Table 4. Compositions measured by SEM EDX from the areas shown in Figure 11, given in atomic percent. The carbon content is overestimated due to hydrocarbon contamination of the sample surface.

| Element/Spectrum	C	N	O	Mg	Al	Si	Ti	Cr	Fe	Ni	Nb	Mo
29	26.9	7.2	25.0	5.5	12.4	-	3.4	4.1	-	7.7	6.9	1.0
30	25.4	-	-	-	0.3	-	0.3	18.8	0.2	45.9	4.0	5.1
31	26.0	-	-	-	0.1	0.3	0.2	19.7	0.2	47.5	1.7	3.8
32	46.2	-	16.0	-	0.9	0.1	2.7	5.7	-	11.8	14.9	1.7
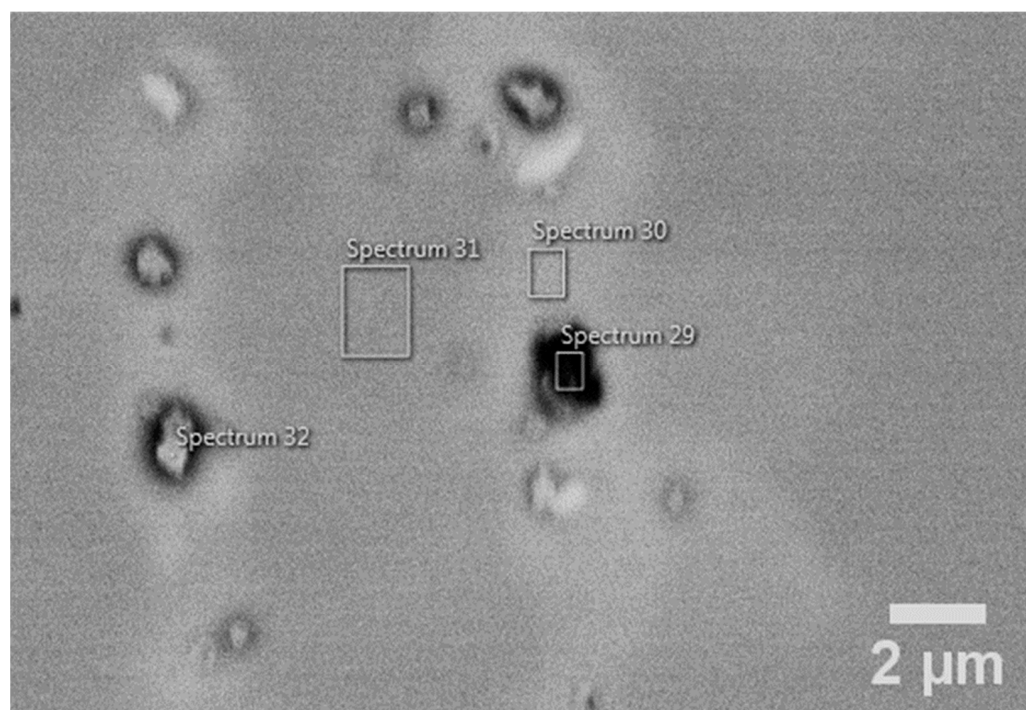
Figure 11. SEM BSE image of a cross-section near the middle of W3. Regions rich in Nb and Mo (spectrum 30) can be distinguished by the higher intensity in the image. Chemical composition measured in the indicated regions are given in Table 4.

To be able to identify the particles found in the interdendritic regions, TEM was used for more detailed chemical and structural analysis. Figure 12 shows a high-angle annular dark-field (HAADF) STEM image from the middle of W2. As shown in the image, particles had often nucleated on other particles. Three different types of particles were identified based on TEM.

**Table 5.** Compositions measured by STEM-EDX from the areas indicated in Figure 12, given in atomic percent.

| Element/Spectrum	O	Mg	Al	Ti	Cr	Fe	Ni	Nb	Mo
1	-	-	-	6.3	14.7	0.3	32.4	41.9	4.4
2	38.1	7.0	41.3	6.4	1.5	-	2.1	3.7	-
3	7.7	-	-	17.7	13.8	-	30.4	28.0	2.4
4	50.1	5.1	19.0	4.7	1.1	-	1.6	17.7	0.8
5	4.0	-	-	5.8	7.5	-	13.6	65.3	3.9
6	-	-	-	-	26.1	0.5	63.7	4.1	5.6
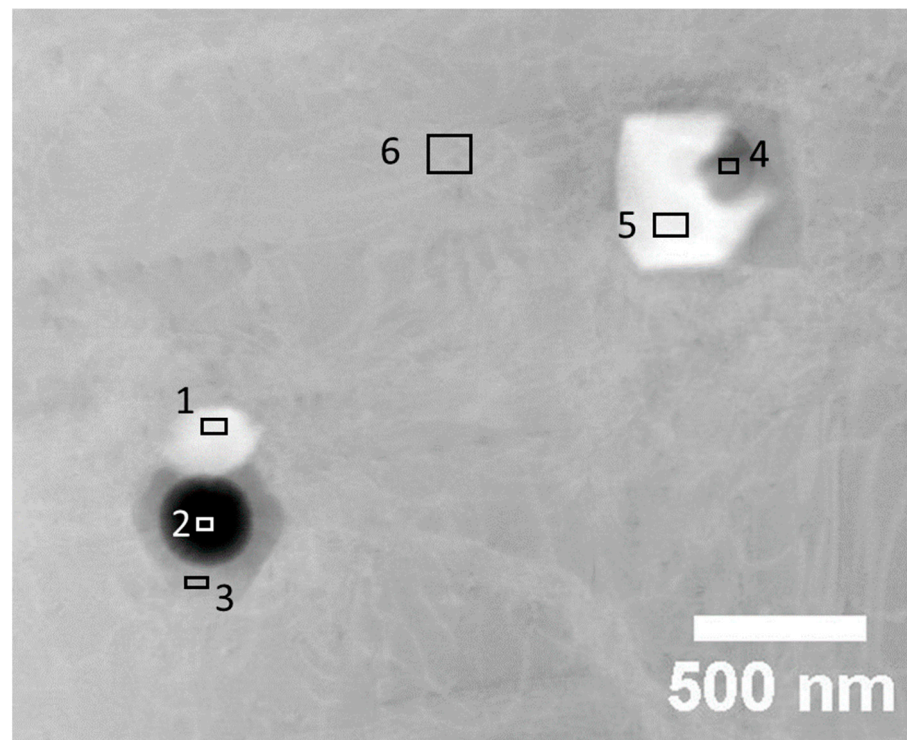
Figure 12. HAADF STEM image of particles in the middle of W2. Compositions from the indicated regions measured by STEM-EDX are given in Table 5.

The first type of particle typically had a spherical morphology and contained Al, O, and some Mg. Based on the chemical composition, and combined with selected-area electron diffraction patterns (Figure 13), these particles could be identified as spinel ($MgAl_2O_4$, space group Fd-3m, lattice parameter a = 8.08 Å [43]). The Mg content measured by STEM-EDX was lower than expected for spinel. However, the composition of spinel can deviate significantly from its stoichiometric composition [44].

Some of the spinel particles were surrounded by disc-shaped particles, as seen in Figures 12 and 13a. This second type of particles could, using selected-area electron diffraction (Figure 13c and combined EDX/EELS mapping (Figure 14)), be identified as the NbTiCN phase (space group Fm-3m, a = 4.363 Å [45]). This phase has a lattice parameter close to half the lattice parameter of spinel. As can be seen in the diffraction pattern in Figure 13c, the spinel particle and the NbTiCN particle have the same orientation, suggesting that the interface between them is partially coherent.
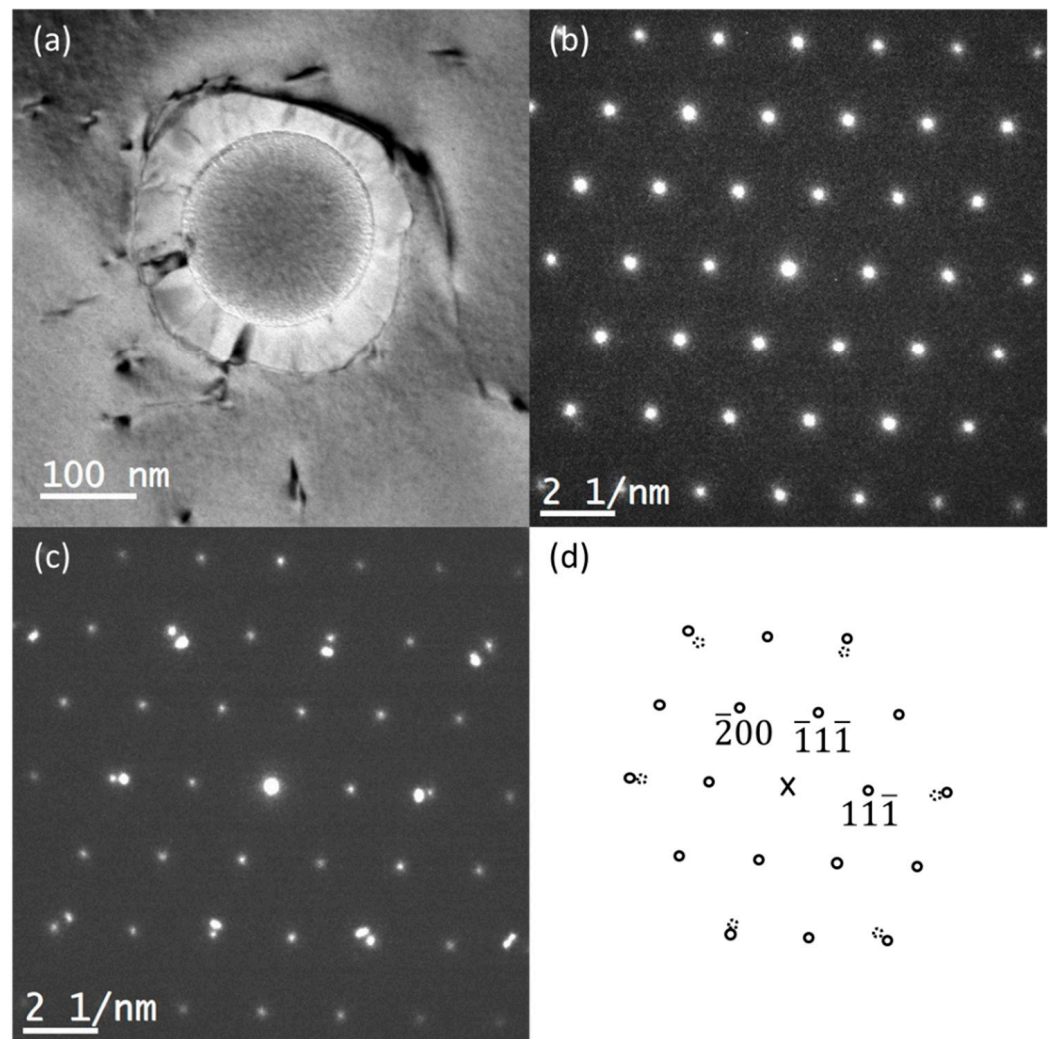
Figure 13. (**a**) Bright-field TEM image of a spinel particle surrounded by a NbTiCN particle in W2. (**b**) SAED pattern from the centre of the spinel sphere on the [011] zone axis. (**c**) SAED pattern from a region including both spinel and NbTiCN, acquired under the same conditions as in (**b**). (**d**) Schematic of the central part of the diffraction pattern in (**c**). Reflections due to spinel and NbTiCN are indicated by full and dashed circles, respectively. The Miller indices of three of the spinel reflections are given. The forbidden 200 reflections are present due to dynamical diffraction.
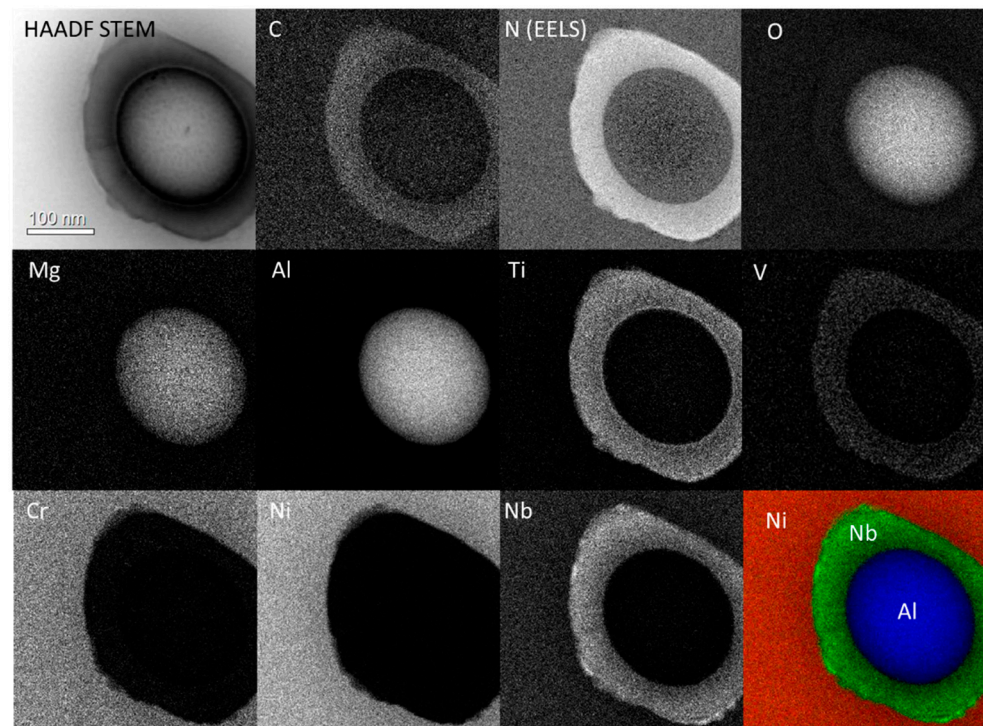
Figure 14. HAADF STEM image and elemental composition maps of spinel/NbTiCN particles in W2. The elemental maps were acquired with EDX, except for N, which was acquired by EELS. The lower-right image is a red–green–blue colour composite of the Ni, Nb and Al maps. The elliptical shape of the spinel particle is due to sample drift during acquisition.

All EBSD patterns were first indexed using Hough indexing, assuming that all patterns match NiCr. The orientations obtained from Hough indexing show good matches between experimental and simulated patterns from NiCr in Figure 15a,b for the green and red grain, respectively. Four spherical regions of low similarity to their neighbouring pixels were identified manually in the ADP map and are highlighted in white circles in Figure 15. The averaged pattern from each of these regions, shown in Figure 15c–f, was compared to dynamically simulated patterns from the four candidate phases obtained from the TEM results: NiCr, NbTiCN, Spinel $MgAl_2O_4$, and CrNbNi. The comparison was performed via dictionary indexing (DI). The phase best matching the patterns in Figure 15d,e is Spinel, while the phase best matching the patterns in Figure 15c,f is NiCr, as shown by their having the two highest NCC scores, *r*, for the best and next-best matching phases. However, the patterns in Figure 15c,f contain Kikuchi bands from two or more crystals, and the next-best matching phases are NbTiCN and spinel, respectively.
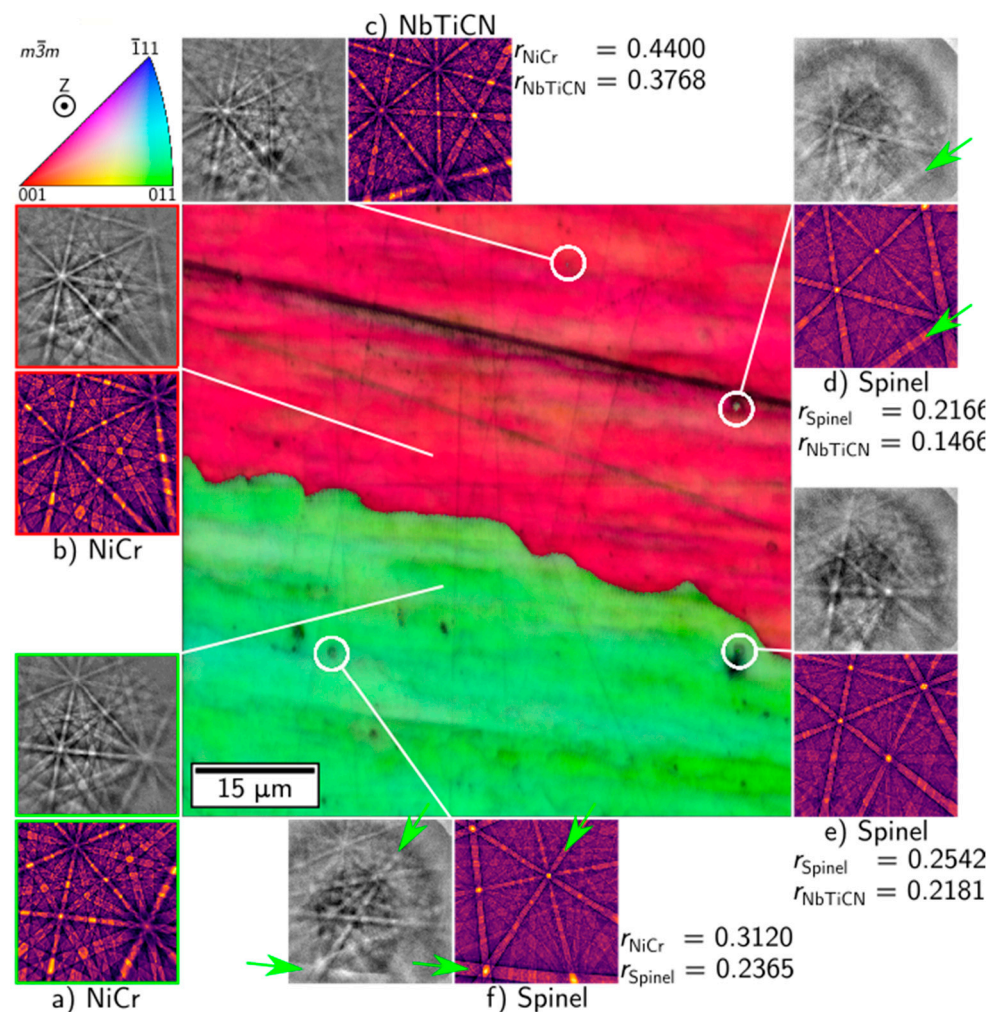
Figure 15. Orientation map from a boundary between two grains as well as experimental and simulated EBSD patterns from selected locations in W2: (**a**) the matrix of the green grain (**b**) the matrix of the red grain (**c**) a NbTiCN particle (**d**–**f**) spinel particles. The green arrows indicate some of the bands coming from spinel.

4. Conclusions

The present study was initiated to study the properties of the WAAM of Inconel 625. The following conclusions can be drawn:

1. The hardness increases from the base metal level of 210, via the HAZ, with HV10 of 220, to the weld fused metal, with a hardness of around 240–250.
2. The hardness was almost independent of the heat input within the current variation range.
3. The Charpy V notch toughness was excellent, with variation between 160 and 200 J.
4. The fracture toughness (CTOD) fell within a range of 0.49 to 1.05 mm.
5. Columnar dendritic solidification took place with heavy microsegregation of Mo and Nb to liquid interdendritic regions, and enrichment of Ni, Cr and possibly Fein primary dendrites.
6. Interdendritic regions contained particles like spinel ($MgAl_2O_4$). These were often surrounded by NbTiCN phase with the same orientation as spinel, suggesting that the interface between them is partially coherent.

Institutional Review Board Statement: Not applicable.

Informed Consent Statement: Not applicable.

Data Availability Statement: Data available on request.

Conflicts of Interest: The authors declare no conflict of interest.

References

1. Martina, F.; Mehnen, J.; Williams, S.W.; Colegrove, P.; Wang, F. Investigation of the benefits of plasma deposition for the additive layer manufacture of Ti–6Al–4V. *J. Mater. Process. Technol.* **2012**, *212*, 1377–1386. [CrossRef]
2. Szost, B.A.; Terzi, S.; Martina, F.; Boisselier, D.; Prytuliak, A.; Pirling, T.; Hofmann, M.; Jarvis, D.J. A comparative study of additive manufacturing techniques: Residual stress and microstructural analysis of CLAD and WAAM printed Ti–6Al–4V components. *Mater. Des.* **2016**, *89*, 559–567. [CrossRef]
3. Williams, S.W.; Martina, F.; Addison, A.C.; Ding, J.; Pardal, G.; Colegrove, P. Wire plus Arc Additive Manufacturing. *Mater. Sci. Technol.* **2016**, *32*, 641–647. [CrossRef]
4. *ISO/ASTM 52900:2021*; Additive Manufacturing—General Principles—Fundamentals and Vocabulary. International Organization for Standardization: Geneva, Switzerland, 2021.
5. Fang, X.; Zhang, L.; Li, H.; Li, C.; Huang, K.; Lu, B. Microstructure Evolution and Mechanical Behavior of 2219 Aluminum Alloys Additively Fabricated by the Cold Metal Transfer Process. *Materials* **2018**, *11*, 812. [CrossRef] [PubMed]
6. Fang, X.; Zhang, L.; Chen, G.; Dang, X.; Huang, K.; Wang, L.; Lu, B. Correlations between Microstructure Characteristics and Mechanical Properties in 5183 Aluminium Alloy Fabricated by Wire-Arc Additive Manufacturing with Different Arc Modes. *Materials* **2018**, *11*, 2075. [CrossRef]
7. Cong, B.; Qi, Z.; Qi, B.; Sun, H.; Zhao, G.; Ding, J. A Comparative Study of Additively Manufactured Thin Wall and Block Structure with Al-6.3%Cu Alloy Using Cold Metal Transfer Process. *Appl. Sci.* **2017**, *7*, 275. [CrossRef]
8. Cong, B.; Ding, J.; Williams, S. Effect of arc mode in cold metal transfer process on porosity of additively manufactured Al-6.3% Cu alloy. *Int. J. Adv. Manuf. Technol.* **2015**, *76*, 1593–1606. [CrossRef]
9. Horgar, A.; Fostervoll, H.; Nyhus, B.; Ren, X.; Eriksson, M.; Akselsen, O.M. Additive manufacturing using WAAM with AA5183 wire. *J. Mater. Process. Technol.* **2018**, *259*, 68–74. [CrossRef]
10. Wu, B.; Ding, D.; Pan, Z.; Cuiuri, D.; Li, H.; Han, J.; Fei, Z. Effects of heat accumulation on the arc characteristics and metal transfer behavior in Wire Arc Additive Manufacturing of Ti6Al4V. *J. Mater. Process. Technol.* **2017**, *250*, 304–312. [CrossRef]
11. Martina, F.; Colegrove, P.A.; Williams, S.W.; Meyer, J. Microstructure of Interpass Rolled Wire + Arc Additive Manufacturing Ti-6Al-4V Components. *Metall. Mater. Trans. A* **2015**, *46*, 6103–6118. [CrossRef]
12. Haden, C.V.; Zeng, G.; Carter, F.M.; Ruhl, C.; Krick, B.A.; Harlow, D.G. Wire and arc additive manufactured steel: Tensile and wear properties. *Addit. Manuf.* **2017**, *16*, 115–123. [CrossRef]
13. Ji, L.; Lu, J.; Liu, C.; Jing, C.; Fan, H.; Ma, S. Microstructure and mechanical properties of 304 L steel fabricated by arc additive manufacturing. *MATEC Web Conf.* **2017**, *128*, 2017. [CrossRef]
14. Rodriguez, N.; Vázquez, L.; Huarte, I.; Arruti, E.; Tabernero, I.; Alvarez, P. Wire and arc additive manufacturing: A comparison between CMT and TopTIG processes applied to stainless steel. *Weld. World* **2018**, *62*, 1083–1096. [CrossRef]
15. Martina, F.; Ding, J.; Williams, S.; Caballero, A.; Pardal, G.; Quintino, L. Tandem metal inert gas process for high productivity wire arc additive manufacturing in stainless steel. *Addit. Manuf.* **2019**, *25*, 545–550. [CrossRef]
16. Caballero, A.; Ding, J.; Ganguly, S.; Williams, S. Wire + Arc Additive Manufacture of 17-4 PH stainless steel: Effect of different processing conditions on microstructure, hardness, and tensile strength. *J. Mater. Process. Technol.* **2018**, *268*, 54–62. [CrossRef]
17. Eriksson, M.; Lervik, M.; Sørensen, C.; Robertstad, A.; Brønstad, B.M.; Nyhus, B.; Aune, R.; Ren, X.; Akselsen, O.M. Additive manufacture of superduplex stainless steel using WAAM. *MATEC Web Conf.* **2018**, *188*, 03014. [CrossRef]
18. Akselsen, O.M.; Bjørge, R.; Anes, H.W.; Ren, X.; Nyhus, B. Effect of Sigma Phase in Wire Arc Additive Manufacturing of Superduplex Stainless Steel. *Metals* **2021**, *11*, 2045. [CrossRef]
19. Shankar, V.; Rao, K.B.S.; Mannan, S.L. Microstructure and mechanical properties of Inconel 625 superalloy. *J. Nucl. Mater.* **2001**, *288*, 222–232. [CrossRef]
20. Shankar, V.; Valsan, M.; Rao, K.B.S.; Mannan, S.L. Effects of temperature and strain rate on tensile properties and activation energy for dynamic strain aging in alloy 625. *Metall. Mater. Trans.* **2004**, *35A*, 3129–3139. [CrossRef]

21. Xu, F.; Lv, Y.; Liu, Y.; Shu, F.; He, P.; Xu, B. Microstructural evolution and mechanical properties of Inconel 625 alloy during pulsed plasma arc deposition process. *J. Mater. Sci. Technol.* **2013**, *29*, 480–488. [CrossRef]

22. Asala, G.; Khan, A.K.; Andersson, J.; Ojo, O.A. Microstructural Analyses of ATI 718Plus® Produced by Wire-ARC Additive Manufacturing Process. *Metall. Mater. Trans.* **2017**, *48A*, 4211–4228. [CrossRef]

23. Cozar, R.; Pineau, A. Morphology of γ' and γ'' precipitates and thermal stability of Inconel 718 type alloys. *Metall. Trans.* **1973**, *4*, 47–59. [CrossRef]

24. Xie, X.; Dong, J.; Wang, G.; You, W. The Effect of Nb, Ti, Al on Precipitation and Strengthening Behavior of 718 Type Superalloys. In *Superalloys 718, 625, 706 and Derivatives*; Loria, E.A., Ed.; TMS, The Minerals, Metals & Materials Society: Pittsburgh, PA, USA, 2005; pp. 287–298.

25. Thivillon, L.; Bertrand, P.H.; Laget, B.; Smurov, I. Potential of direct metal deposition technology for manufacturing thick functionally graded coatings and parts for reactors components. *J. Nucl. Mater.* **2009**, *385*, 236–241. [CrossRef]

26. Chen, Y.H.; Park, S.U.; Wei, D.; Newstadt, G.; Jackson, M.A.; Simmons, J.P.; de Graef, M.; Hero, A.O. A dictionary approach to electron backscatter diffraction indexing. *Microsc. Microanal.* **2015**, *21*, 739–752. [CrossRef] [PubMed]

27. Ånes, H.W.; Natlandsmyr, O.; Bergh, T.; Lervik, L. Pyxem/Kikuchipy: Kikuchipy 0.4.0 (v0.4.0). *Zenodo* **2021**. [CrossRef]

28. Callahan, P.G.; de Graef, M. Dynamical Electron Backscatter Diffraction Patterns. Part I: Pattern Simulations. *Microsc. Microanal.* **2013**, *19*, 1255–1265. [CrossRef] [PubMed]

29. Singh, S.; de Graef, M. Orientation sampling for dictionary-based diffraction pattern indexing methods. *Model. Simul. Mater. Sci. Eng.* **2016**, *24*, 085013. [CrossRef]

30. Virtanen, P.; Gommers, R.; Oliphant, T.E.; Haberland, M.; Reddy, T.; Cournapeau, D.; Burovski, E.; Peterson, P.; Weckesser, W.; Bright, J.; et al. SciPy 1.0 Contributors: SciPy 1.0: Fundamental Algorithms for Scientific Computing in Python. *Nat. Methods* **2020**, *17*, 261–272. [CrossRef]

31. Dinda, G.P.; Dasgupta, A.K.; Mazumder, J. Laser aided direct metal deposition of Inconel 625 superalloy: Microstructural evolution and thermal stability. *Mater. Sci. Eng.* **2009**, *A509*, 98–104. [CrossRef]

32. Wang, Y.; Chen, X.; Su, C. Microstructure and mechanical properties of Inconel 625 fabricated by wire-arc additive manufacturing. *Surf. Coat. Technol.* **2019**, *374*, 116–123.

33. Korrapati, P.K.; Avasarala, V.K.; Bhushan, M.; Ramkumar, K.D.; Arivazhagan, N.; Narayanan, N.S. Assessment of Mechanical properties of PCGTA weldments of Inconel 625. *Procedia Eng.* **2014**, *75*, 9–13. [CrossRef]

34. Xu, F.; Lv, Y.; Xu, B.; Liu, Y.; Shu, F.; He, P. Effect of Heat Treatment on Microstructure and Mechanical Properties of Inconel 625 Alloy Fabricated by Pulsed Plasma Arc Deposition. *Phys. Procedia* **2013**, *50*, 48–54. [CrossRef]

35. Xu, F.; Lv, Y.; Liu, Y.; Xu, B.; He, P. Effect of deposition strategy on the microstructure and mechanical properties of Inconel 625 superalloy fabricated by pulsed plasma arc deposition. *Mater. Des.* **2013**, *45*, 446–455. [CrossRef]

36. Wang, J.F.; Sun, Q.J.; Wang, H.; Liu, J.P.; Feng, J.C. Effect of location on microstructure and mechanical properties of additive layer manufactured Inconel 625 using gas tungsten arc welding. *Mater. Sci. Eng.* **2016**, *A676*, 395–405. [CrossRef]

37. Paul, C.P.; Ganesh, P.; Mishra, S.K.; Bhargava, P.; Negi, J.; Nath, A.K. Investigating laser rapid manufacturing for Inconel-625 components. *Opt. Laser Technol.* **2007**, *39*, 800–805. [CrossRef]

38. Puppala, G.; Moitra, A.; Sathyanarayanan, S.; Kaul, R.; Sasikala, G.; Prasad, R.C.; Kukreja, L.M. Evaluation of fracture toughness and impact toughness of laser rapid manufactured Inconel-625 structures and their co-relation. *Mater. Des.* **2014**, *59*, 509–515. [CrossRef]

39. Cam, G.; dos Santos, J.F.; Kocak, M. Properties of laser beam welded superalloys Inconel 625 and 718. In Proceedings of the European Conference on Laser Treatment of Materials, Hannover, Germany, 22–23 September 1998; pp. 333–338.

40. Yeni, C.; Kocak, M. Fracture toughness analysis of laser-beam-welded super alloys Inconel 718 and 625. *Fatigue Fract. Eng. Mater. Struct.* **2006**, *29*, 546–557. [CrossRef]

41. Floreen, S.; Fuchs, G.E.; Yang, W.J. The metallurgy of alloy 625. In *Superalloys 718, 625, 706 and Various Derivatives*; Loria, E.A., Ed.; TMS, The Minerals, Metals & Materials Society: Pittsburgh, PA, USA, 1994; pp. 13–37.

42. ASM Metals Handbook Committee. *ASM Metals Handbook. Properties and Selection: Nonferrous Alloys and Special-Purpose Materials*, 9th ed.; ASM: Metals Park, OH, USA, 1980; Volume 3, p. 142.

43. Yamanaka, T.; Takeuchi, Y. Order-disorder transition in $MgAl_2O_4$ spinel at high temperatures up to 1700 °C. *Z. Krist.* **1983**, *165*, 65–78. [CrossRef]

44. Murphy, S.T.; Gilbert, C.A.; Smith, R.; Mitchell, T.E.; Grimes, R.W. Non-stoichiometry in $MgAl_2O_4$ spinel. *Phil. Mag.* **2010**, *90*, 1297–1305. [CrossRef]

45. Kieffer, R.; Ettmayer, P.; Dufek, G.; Nowotny, H. Recent investigations on the miscibility of transition element nitrides and carbides. *Metall* **1972**, *26*, 701–708.

46. Will, G.; Platzbecker, R. Crystal Structure and Electron Density Distribution in Niobium Carbide. *Z. Anorg. Allg. Chem.* **2001**, *627*, 2207–2210. [CrossRef]